

# Thermal instability (or not?) in three-dimensional, global, radiative GRMHD simulations of geometrically thin discs

B. Mishra<sup>1\*</sup>, P. C. Fragile<sup>2</sup>, L. C. Johnson<sup>2</sup>, W. Kluźniak<sup>1</sup>

<sup>1</sup>*Nicolaus Copernicus Astronomical Center, Bartycka 18, Warsaw, 00-716, Poland*

<sup>2</sup>*Department of Physics and Astronomy, College of Charleston, 66 George Street, Charleston SC 29424, USA*

Accepted \*\*\* Received \*\*\*

## ABSTRACT

We present results of a set of three-dimensional, general relativistic radiation magnetohydrodynamics simulations of thin accretion discs to test their thermal stability. We consider two cases, one that is initially radiation-pressure dominated and expected to be thermally unstable and another that is initially gas-pressure dominated and expected to remain stable. Indeed, we find that cooling dominates over heating in the radiation-pressure-dominated case, causing the disc to collapse vertically on the local cooling timescale. On the other hand, the gas-pressure-dominated case, which was run for twice as long as the radiation-pressure-dominated case, remains stable, with heating and cooling roughly in balance. Because the radiation-pressure-dominated disc collapses to the point that we are no longer able to resolve it, we had to terminate the simulation. Thus, we do not know for sure whether it might find a much thinner, stable solution or if it will make a transition to unstable expansion and exhibit limit-cycle behavior. However, the fact that the cooling rate seems to be dropping faster than heating as the disc collapses suggests that the disc may be headed toward a stable, albeit thinner, solution. It is not clear, though, if the disc will remain radiation-pressure-dominated in that new state.

**Key words:** accretion, accretion discs – black hole physics – instabilities – MHD – radiation: dynamics

## 1 INTRODUCTION

It has been over forty years since the seminal paper on geometrically thin accretion discs was published by Shakura & Sunyaev (1973). This model prescribed three different regions in such discs: a radiation-pressure-dominated (inner) region, with the dominant opacity due to electron scattering; a gas-pressure-dominated (middle) region, with the dominant opacity again due to electron scattering; and a gas-pressure-dominated (outer) region, with opacity due to free-free absorption. Soon after publication, linear stability analysis of the radiation-pressure-dominated region indicated that it should be unstable (Shakura & Sunyaev 1976).

The origin of this instability is the assumption that the anomalous stress,  $\tau_{\theta}$ , that drives accretion is proportional to the total (gas plus radiation) pressure. This actually leads to two instabilities, one being thermal (Shakura & Sunyaev 1976) and the other viscous (Lightman & Eardley 1974). In this work we are mainly focused on the thermal instability. The necessary and sufficient condition proposed by Piran (1978) shows that the thermal instability originates due to the different dependence of the heating and cooling rates per unit area on the disc mid-plane temperature, for a constant surface density,  $\Sigma$ . The ratio of heating rate per unit area to cooling rate per unit area is proportional to the fourth power of the

mid-plane temperature (Piran 1978). This leads to excess heating, resulting in an expanding disc. In numerical simulations, it can also happen that cooling dominates heating, such that the disc collapses (Jiang, Stone & Davis 2013; Sądowski 2016). All of this assumes that any magnetic fields in the disc are weak. If strong magnetic fields are present, they can, in principle, stabilize the disc (Begelman & Pringle 2007; Oda et al. 2009; Sądowski 2016).

In recent years, local, shearing-box (Brandenburg et al. 1995; Stone et al. 1996) numerical simulations have been performed to study the thermal stability of radiation-pressure-dominated discs (Turner 2004; Hirose, Krolik & Blaes 2009; Jiang, Stone & Davis 2013). The first radiation MHD simulation using a stratified shearing box was performed by Turner (2004). In this simulation, even with a radiation-to-gas pressure ratio of  $\sim 14$ , the disc did not show any thermal instability. However, these results are suspect, due to the fact that the photosphere was not captured within the simulation domain (during the expansion phase caused by heating). Furthermore, half of the mass was lost from the boundaries of the simulation box and 27% of work done on the box disappeared due to numerical losses. Hirose, Krolik & Blaes (2009) repeated the radiation-pressure-dominated shearing box simulations with a better energy conservation scheme and larger box to retain both (top and bottom) photospheres within the simulation domain. They also greatly reduced the mass loss through the box boundaries. These simulations, too, showed no thermal instability. The analytic and

\* E-mail: mbhupe@camk.edu.pl

numerical results were thus in conflict until new shearing box simulations were performed by Jiang, Stone & Davis (2013). Depending on the central density and the ratio of radiation pressure to gas pressure, Jiang, Stone & Davis (2013) found all of their discs to either expand or collapse on a timescale of tens of orbits. They were also able to demonstrate that the previous contradictory results were owing to the use of too small boxes.

We expand the previous shearing box results into the domain of global simulations using the *Cosmos++* general relativistic radiation magnetohydrodynamic (GRRMHD) code (Anninos, Fragile & Salmonson 2005; Fragile et al. 2012; Fragile, Olejar & Anninos 2014). We compare two general cases, one gas-pressure-dominated, the other radiation-pressure-dominated. The radiation-pressure-dominated case has parameters chosen to closely match those of one of the unstable shearing-box cases of Jiang, Stone & Davis (2013).

## 2 NUMERICAL SETUP

### 2.1 Initial configurations

In order to make connections with previous shearing box (esp. Jiang, Stone & Davis 2013) and global, thin-disc (Reynolds & Miller 2009) simulations, instead of starting from the Shakura-Sunyaev solution, we initialized a slab of gas of uniform thickness, orbiting everywhere at the local Keplerian frequency. We chose a black hole mass,  $M_{\text{BH}} = 6.62M_{\odot}$ , for close comparison with Jiang, Stone & Davis (2013). The initial density profile of the azimuthally symmetric disc is

$$\rho(R, z) = \frac{\rho_0 e^{-z^2/2H^2}}{1 + e^{(R_i - R)/H}}, \quad (1)$$

where  $\rho_0$  is the mid-plane density,  $H$  is the initial height of the disc, and  $R_i$  is the inner radius of the initial disc. We fix the initial inner radius to that of the innermost stable circular orbit (ISCO) and use an exponential cutoff to smooth the transition there. The initial disc structure is thus entirely governed by the chosen mid-plane density and disc height. We consider two cases, one with mid-plane density  $\rho_0 = 10^{-3} \text{ g cm}^{-3}$  and  $H = 0.4r_g$ , where  $r_g = GM/c^2$  is the gravitational radius, and the other with  $\rho_0 = 10^{-6} \text{ g cm}^{-3}$  and  $H = 0.3r_g$ . The first case matches the RSVET model in the shearing-box simulations of Jiang, Stone & Davis (2013). The Jiang, Stone & Davis (2013) simulations were done for a section of disc centered at  $R = 30r_g$ , whereas we are performing global simulations, so the correspondence is imperfect. In our case, the disc is initially radiation pressure dominated, with  $10 \lesssim P_{\text{rad}}/P_{\text{gas}} \lesssim 1000$ . We refer to this setup as RADPLR or RADPHR depending on the resolution used (see Table 1).

For RADPHR and RADPLR, we assume that the gas and radiation are initially in local thermal equilibrium (LTE), which means the total pressure is distributed between the two (magnetic pressure is initially negligible), as

$$P_{\text{tot}} = P_{\text{gas}} + P_{\text{rad}}, \quad (2)$$

where the total pressure,  $P_{\text{tot}}$ , is defined by the disc vertical equilibrium equation

$$P_{\text{tot}} = \frac{GM_{\text{BH}}H^2}{R(R - 2r_g)^2} \rho(R, z). \quad (3)$$

Substituting the expressions for radiation pressure (in local thermodynamic equilibrium) and ideal gas pressure into equation (2), we have

$$\frac{1}{3}a_{\text{R}}T_{\text{gas}}^4 + \frac{k_{\text{b}}\rho T_{\text{gas}}}{\mu} - P_{\text{tot}} = 0, \quad (4)$$

where  $a_{\text{R}} = 4\sigma/c$  is the radiation constant. This is a quartic equation for the gas temperature with four possible roots, though only one is positive and real.

The second case we consider is somewhat different in terms of its thermodynamic properties. This lower density case is gas pressure dominated, with  $10^{-11} \lesssim P_{\text{rad}}/P_{\text{gas}} \lesssim 10^{-7}$  for entire disc. We refer to this setup as GASPLR or GASPHR, again depending on the resolution (Table 1). GASPHR and GASPLR have an initial disc thickness  $H = 0.3r_g$ . In this case, we do not assume LTE, initially. Instead, we define a uniform, initial radiation temperature,  $T_{\text{rad}} = 10^4 \text{ K}$ , considerably below the initial gas temperature.

### 2.2 Radiation fields

The  $\mathbf{M}_1$  closure scheme in *Cosmos++* (Fragile, Olejar & Anninos 2014) evolves the radiation energy density in the radiation rest frame,  $E_{\text{R}}$ , and the spatial components of the radiation rest frame 4-velocity,  $u_{\text{R}}^i$  (see Section 2.5). However, it is easier to initialize our simulations by defining the radiation fields in the fluid frame. We already described in the previous section how we determine the initial radiation temperature,  $T_{\text{rad}}$ . This temperature can be used to define the radiation energy density in the fluid frame

$$E_{\text{rad}} = a_{\text{R}}T_{\text{rad}}^4. \quad (5)$$

The initial radiative flux,  $F^i$ , is then calculated from the gradient of  $E_{\text{rad}}$ . With these quantities, we can construct the contravariant radiation stress-energy tensor

$$R^{\alpha\beta} = E_{\text{rad}}u^{\alpha}u^{\beta} + F^{\alpha}u^{\beta} + F^{\beta}u^{\alpha} + \frac{1}{3}E_{\text{rad}}h^{\alpha\beta}, \quad (6)$$

where  $h^{\alpha\beta} = g^{\alpha\beta} + u^{\alpha}u^{\beta}$  is the projection tensor and  $u^{\alpha}$  is the fluid 4-velocity.

Since the radiation stress-energy tensor is invariant, it must be the same in all frames. This allows us to equate the radiation stress-energy tensor from equation (6) to the form written in terms of the radiation rest frame variables:

$$R^{\alpha\beta} = \frac{4}{3}E_{\text{R}}u_{\text{R}}^{\alpha}u_{\text{R}}^{\beta} + \frac{1}{3}E_{\text{R}}g^{\alpha\beta}. \quad (7)$$

Following Sądowski et al. (2013) and Fragile, Olejar & Anninos (2014), we start with the following two relationships, both of which come from equation (7):

$$g_{\alpha\beta}R^{\alpha}R^{\beta} = -\frac{8}{9}E_{\text{R}}^2(u_{\text{R}}^t)^2 + \frac{1}{9}E_{\text{R}}^2g^{tt} \quad (8)$$

and

$$R^{tt} = \frac{4}{3}E_{\text{R}}(u_{\text{R}}^t)^2 + \frac{1}{3}E_{\text{R}}g^{tt}. \quad (9)$$

Using these, we solve for the radiation energy density in the radiation rest frame,  $E_{\text{R}}$ , and the time component of the radiation rest frame four-velocity,  $u_{\text{R}}^t$ . With these, the remaining spatial components of the radiation rest frame 4-velocity,  $u_{\text{R}}^i$ , can easily be obtained from equation (7).

### 2.3 Magnetic field setup

To seed the magneto-rotational instability (MRI) inside the disc, we impose a weak magnetic field ( $\beta = P_{\text{tot}}/P_{\text{mag}} \geq 10$ ) on top of our hydrodynamical setup. The MRI is necessary to drive the accretion

of matter into the black hole and transport angular momentum outwards (Balbus & Hawley 1991). The turbulence of the MRI will also heat the disc, which is important to our goal of studying thermal stability.

It is important for the initialized magnetic field to be divergence free. The easiest way to accomplish this is to initialize the magnetic field starting from the vector potential. For our thin discs, we set  $A_r = A_z = 0$  and

$$A_\phi = \frac{\sqrt{P_{\text{gas}}} \sin(2\pi R/5H)}{1 + e^\Delta}, \quad (10)$$

where

$$\Delta = 10 \left\{ \frac{z^2}{H^2} + \left( \frac{H}{R - R_{\text{ISCO}}} \right)^2 - 1 \right\} \quad (11)$$

and  $R_{\text{ISCO}}$  is the radius of the ISCO. The effect is to create small magnetic field loops of roughly the same size as the disc height and alternating polarity centered along the mid-plane of the disc. The generalized curl of the vector potential

$$\mathcal{B}^i = \epsilon^{ijk} \partial_j A_k \quad (12)$$

then gives the appropriate magnetic field components. The strength of the magnetic field is scaled to match the chosen  $\beta$ . In order to keep the magnetic field divergence free during the evolution, we use the staggered, *constrained transport* scheme described in Fragile et al. (2012).

## 2.4 Grid parameters

In thin-disc simulations, a big challenge is to have enough resolution to capture the MRI. To help with this, we adopt a cylindrical, Kerr-Schild coordinate system computed by transformation from the usual spherical Kerr-Schild coordinate system ( $R = r \sin \theta$  and  $z = r \cos \theta$ ). To further improve the resolution near the disc mid-plane, we space the  $n_z = 160$  zones using a logarithmic coordinate

$$x_3 = \pm \ln \left( \frac{n_z |z| - L_z}{L_z} \right), \quad (13)$$

where  $L_z = 20H$  is the total box height and the sign of the expression comes from the sign of  $z$ . We also employ a logarithmic grid in the radial direction with  $n_R = 192$  zones spaced as

$$x_1 = 1 + \ln \left( \frac{R}{r_{\text{BH}}} \right), \quad (14)$$

where  $r_{\text{BH}}$  is the black hole radius. The radial domain runs over  $4r_g \leq R \leq 40r_g$ . A linear spacing is used along the azimuthal direction,  $\phi$ , with  $n_\phi = 32$  (low resolution) or  $n_\phi = 64$  (high resolution). To reduce the computational expense we only simulate the  $0 \leq \phi \leq 0.5\pi$  wedge in the azimuthal direction.

We use outflow boundary conditions in the inner radial and top and bottom vertical boundaries, which means all the gas variables except the normal component of the flow velocity are copied from the last active zones to the ghost zones. If the normal velocity component points outward, then it, too, is copied to the ghost zone. Otherwise, it is adjusted such that the normal component of the velocity is zero at the boundary face. The outer radial boundary uses a constant boundary condition, which means that all variables will retain their initial values in the outer radial ghost zones. The azimuthal boundary conditions are periodic.

**Table 1.** Simulation parameters for the four models considered. The model names reflect whether the simulation is radiation- (RADP) or gas- (GASP) pressure dominated and high (HR) or low (LR) resolution. The number of shells along the radial,  $n_R = 192$ , and vertical,  $n_z = 160$ , directions are fixed for all four cases.

| Model  | $\rho_0$<br>( $\text{g cm}^{-3}$ ) | $P_{\text{rad}}/P_{\text{gas}}$ | $192 \times n_\phi \times 160$ |
|--------|------------------------------------|---------------------------------|--------------------------------|
| RADPHR | $10^{-3}$                          | 200                             | 64                             |
| RADPLR | $10^{-3}$                          | 200                             | 32                             |
| GASPHR | $10^{-6}$                          | $10^{-7}$                       | 64                             |
| GASPLR | $10^{-6}$                          | $10^{-7}$                       | 32                             |

## 2.5 Radiative GRMHD scheme

We solve the coupled radiative magnetohydrodynamics equations using the  $\mathbf{M}_1$  closure scheme to handle both the optically thick and thin limits (Fragile, Olejar & Anninos 2014). Along with the radiation stress-energy tensor, defined in equation (7), we need the MHD stress-energy tensor

$$T^{\alpha\beta} = (\rho + \rho\varepsilon + P_{\text{gas}} + b^2) u^\alpha u^\beta + (P_{\text{gas}} + P_{\text{mag}}) g^{\alpha\beta} - b^\alpha b^\beta, \quad (15)$$

where  $\rho$  is rest mass density,  $\varepsilon$  is specific internal energy,  $P_{\text{gas}}$  is gas pressure, defined using the ideal gas equation of state,  $P_{\text{gas}} = (\gamma - 1)\rho\varepsilon$ , with  $\gamma = 5/3$ , and  $b^\alpha$  is the contravariant magnetic 4-field, measured by an observer co-moving with fluid.

We aim to solve the following set of conservation equations for the mass

$$(\rho u^\beta)_{;\beta} = 0, \quad (16)$$

fluid stress-energy

$$(T^\alpha_\beta)_{;\beta} = G_\alpha, \quad (17)$$

and radiation stress-energy

$$(R^\alpha_\beta)_{;\beta} = -G_\alpha, \quad (18)$$

together with the induction equation for the magnetic fields. In equations (17) and (18),  $G_\alpha$  is the radiation 4-force density, which couples the fluid and radiation fields. This term includes normal scattering, absorption, and emission, as well as thermal Comptonization of the radiation. We do not include the relativistic corrections to thermal Comptonization, as we make the simplifying assumption that Compton scattering is symmetric in the fluid frame (hence, there is no associated momentum exchange). The form of  $G^\alpha$  is

$$G^\alpha = A_1 R^{\alpha\nu} u_\nu + (A_2 R^{\mu\nu} u_\mu u_\nu + \kappa_p^a \rho a_R T_{\text{gas}}^4) u^\alpha, \quad (19)$$

where

$$A_1 = -\rho (\kappa_R^a + \kappa^s), \quad (20)$$

$$A_2 = -\rho \left[ \kappa^s + 4\kappa^s \left( \frac{T_{\text{gas}} - T_{\text{rad}}}{m_e} \right) + \kappa_R^a - \kappa_J^a \right], \quad (21)$$

$\kappa_s = 0.34 \text{ cm}^2 \text{ g}^{-1}$  is the opacity due to electron scattering,  $\kappa_R^a = 1.6 \times 10^{21} T^{-7/2} \rho \text{ cm}^2 \text{ g}^{-1}$  is the Rosseland mean of absorption,  $\kappa_J^a$  is the J-mean of absorption, and  $\kappa_P^a$  is the Planck mean of absorption. We assume a nearly Planck spectrum, such that  $\kappa_J^a = \kappa_P^a = 6.4 \times 10^{22} T^{-7/2} \rho \text{ cm}^2 \text{ g}^{-1}$ .  $T_{\text{rad}}$  and  $T_{\text{gas}}$  are the radiation and gas temperatures, respectively. Note that we do not solve independently for the temperature of the electrons, but simply assume it is equal to the temperature of the plasma. This should be sufficient in strongly

coupled systems like the ones we simulate here, although in lower luminosity systems this does not hold (Ressler et al. 2015).

The form of the conservation equations that we actually solve can be written as

$$\partial_t D + \partial_i (DV^i) = 0, \quad (22)$$

$$\partial_t \mathcal{E} + \partial_i (-\sqrt{-g}T_t^i) = -\sqrt{-g}T_{\beta^1\alpha}^{\alpha\beta} - \sqrt{-g}G_t, \quad (23)$$

$$\partial_t \mathcal{S} + \partial_i (\sqrt{-g}T_j^i) = \sqrt{-g}T_{\beta^1\alpha}^{\alpha\beta} + \sqrt{-g}G_j, \quad (24)$$

$$\partial_t \mathcal{R} + \partial_i (\sqrt{-g}R_t^i) = \sqrt{-g}R_{\beta^1\alpha}^{\alpha\beta} - \sqrt{-g}G_t, \quad (25)$$

$$\partial_t \mathcal{R}_j + \partial_i (\sqrt{-g}R_j^i) = \sqrt{-g}R_{\beta^1\alpha}^{\alpha\beta} - \sqrt{-g}G_j, \quad (26)$$

and

$$\partial_t \mathcal{B}^j + \partial_i (\mathcal{B}^j V^i - \mathcal{B}^i V^j) = 0, \quad (27)$$

where  $D = W\rho$  is the generalized fluid density,  $W = \sqrt{-g}u^t$  is the generalized boost,  $V^i = u^i/u^t$  is the fluid transport velocity,  $\mathcal{E} = -\sqrt{-g}T_t^t$  is the total energy density,  $\mathcal{S} = \sqrt{-g}T_j^i$  is the covariant momentum density,  $\mathcal{R} = \sqrt{-g}R_t^i$  and  $\mathcal{R}_j = \sqrt{-g}R_j^i$  are the conserved radiation energy density and momentum, respectively, and  $\mathcal{B}^j = \sqrt{-g}B^j$  is the boosted magnetic field three-vector. The magnetic field,  $B^i = {}^*F^{oi}$ , is related to the co-moving field by

$$B^i = u^0 b^i - u^i b^0, \quad (28)$$

where  ${}^*F^{\alpha\beta}$  is the dual of the Faraday tensor. These equations are solved using the explicit-implicit scheme described in Fragile, Oeljar & Anninos (2014).

### 3 RESULTS

In this section, we present results of our two main simulations. In the first, we find that our geometrically-thin, optically-thick, radiation-pressure-dominated disc collapses vertically on the cooling timescale. The second simulation of an apparently stable, gas-pressure-dominated disc of similar height supports our claim that the first result is not a spurious numerical result.

#### 3.1 Diagnostics

Each simulation is post-processed in order to extract the thermodynamic and geometric properties of the disc. We mainly use density-weighted shell- and time-averaged quantities, as well as space-time diagrams to present our results. A general expression for the density-weighted shell-average of a quantity is given by the following expression:

$$\langle f \rangle_{\rho} = \frac{\int \int f \sqrt{-g}\rho(R, \phi, z) dA_R}{\int \int \sqrt{-g}\rho(R, \phi, z) dA_R}, \quad (29)$$

where  $dA_R$  is an area element normal to the radial direction. A time average of this quantity is computed as

$$\langle f \rangle_{\rho t} = \frac{\int \int f \sqrt{-g}\rho(R, \phi, z, t) dA_R dt}{\int \int \sqrt{-g}\rho(R, \phi, z, t) dA_R dt}. \quad (30)$$

For the height of the disc we use a density-squared weighting:

$$\langle H \rangle_{\rho} = \sqrt{\frac{\int_0^{\pi/2} \int_{z_{\min}}^{z_{\max}} \sqrt{-g}\rho^2(z - z_0)^2 dA_R}{\int_0^{\pi/2} \int_{z_{\min}}^{z_{\max}} \sqrt{-g}\rho^2 dA_R}}, \quad (31)$$

as it agrees better with our target height than other possible expressions, where  $z_0 = 0$  represents the disc mid-plane.

We also track the photosphere of each disc, which we define as the  $\tau = 1$  surface. The optical depth,  $\tau$ , comes from integrating the quantity  $\kappa\rho$  from  $z_{\min}$  to the disc mid-plane and similarly from  $z_{\max}$  to the disc mid-plane:

$$\tau_{<} = \int_{z_{\min}}^0 W\kappa\rho \sqrt{g_{zz}} dz \quad \tau_{>} = \int_0^{z_{\max}} W\kappa\rho \sqrt{g_{zz}} dz, \quad (32)$$

where  $\kappa = \kappa^s + \kappa^a$ . We emphasize here that in our simulations the photosphere is always well within the simulation domain.

The local heating rate due to turbulence caused by the MRI is computed within the volume enclosed by the photosphere by

$$Q^+(R) = \frac{3V^{\phi}T^{R\phi}}{2R} \quad (33)$$

where  $V^{\phi}$  is the azimuthal component of the three velocity and  $T^{R\phi}$  is the contravariant  $R$ - $\phi$  component of the stress-energy tensor. The radiative cooling is computed by tracking the total luminosity escaping from each cylindrical shell. The total cooling rate is thus defined as

$$Q^-(R) = L_{\text{photo}}(R) + L_{\text{radial}}(R), \quad (34)$$

where  $L_{\text{photo}}(R)$  is the luminosity escaping through the photosphere, computed by azimuthally averaging the vertical component of the radiation energy flux,  $R_t^z$ , at a given radius at the photosphere,

$$L_{\text{photo}} = - \int_{\text{photo}} \sqrt{-g}R_t^z dA_z, \quad (35)$$

and  $L_{\text{radial}}$  is the radial luminosity, computed by vertically and azimuthally averaging the radial component of the radiation energy flux,  $R_t^R$ , at a given radius,

$$L_{\text{radial}} = - \int_{\text{shell}} \sqrt{-g}R_t^R dA_R. \quad (36)$$

#### 3.2 Radiation-pressure-dominated disc

The goal of this setup (RADPHR/RADPLR) is to study the thermal stability of a radiation-pressure-dominated disc. Before addressing the thermal stability, though, we present a general overview of this simulation. Fig. 1 shows  $R - z$  slices of the initial (left) vs. final (right) distribution of mass density (upper panel), temperature (middle panel), and the ratio of radiation pressure to gas pressure (lowest panel) for the RADPHR simulation. We clearly see in the upper-right panel that the disc collapses to a very thin structure. The middle-right panel shows that the disc cools down by an order of magnitude with respect to its initial gas temperature. The lower-right panel shows that during the entire simulation the radiation pressure remains dominant within the disc.

In Fig. 2 we show additional  $R - z$  slices of this simulation, now time averaged over the last  $t = 1000 GM/c^3$ . The top panel shows mass density again with streamlines of the azimuthally averaged fluid velocity. The photosphere is shown with cyan solid curves. Again we see that the disc has collapsed to a very thin height. The streamlines also indicate that material is continuing to fall toward the mid-plane. In this case, we terminated the simulation where we did, because we can no longer resolve the disc. The middle panel shows the radiation energy with streamlines of the azimuthally averaged radiation velocity. We see in this panel that the radiation escapes vertically from the disc, which is expected for geometrically thin discs. The lowest panel shows the ratio of

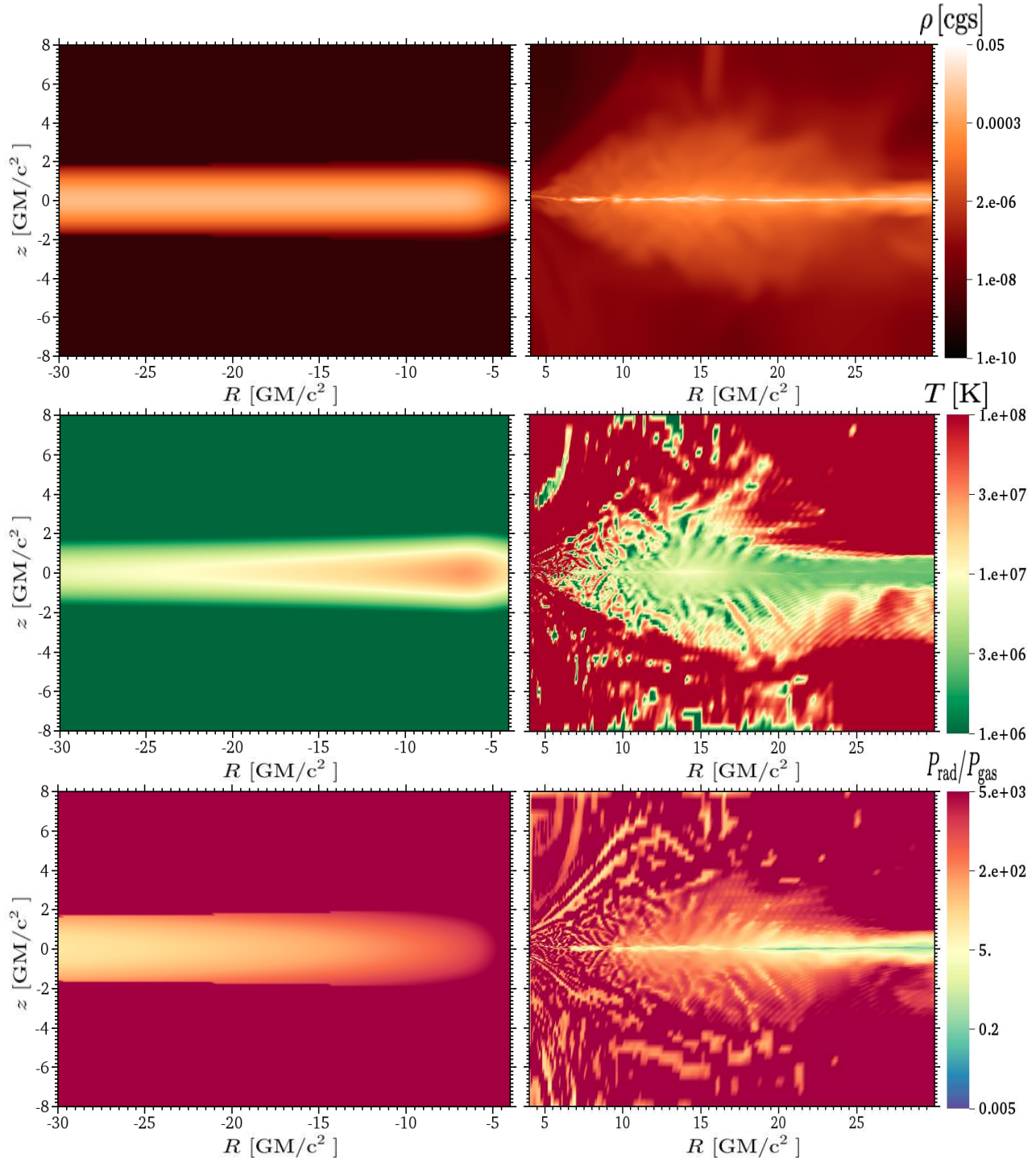


**Figure 1.** An  $R - z$  slice of three-dimensional simulation, RADPHR. The left and right panels correspond, respectively, to the initial and final stages of the simulation. From top to bottom, the panels show mass density, gas temperature, and the ratio of radiation pressure to gas pressure.

the magnetic pressure to the sum of the radiation and gas pressures ( $P_{r+g} = P_{\text{rad}} + P_{\text{gas}}$ ), with streamlines of the azimuthally averaged magnetic field. There is a definite radial structure to the magnetic field lines in the background gas, while the field is more turbulent near the disc mid-plane. Magnetic pressure never dominates in the body of the disc during the entire simulation, though in the background it certainly does. Thus, we do not expect the disc to be stabilized by the magnetic fields.

In Fig. 3 we show a spacetime plot of the azimuthally averaged radial profile of disc height, computed using equation (31). Importantly, the figure shows that the height initially increases after one local MRI growth time, which corresponds to the local orbital timescale (dashed curve). This is due to fact that the MRI is responsible for heating up the disc, allowing it to expand vertically. Subsequently, the disc collapses on a timescale comparable to the local cooling time (solid white curve), which is computed as

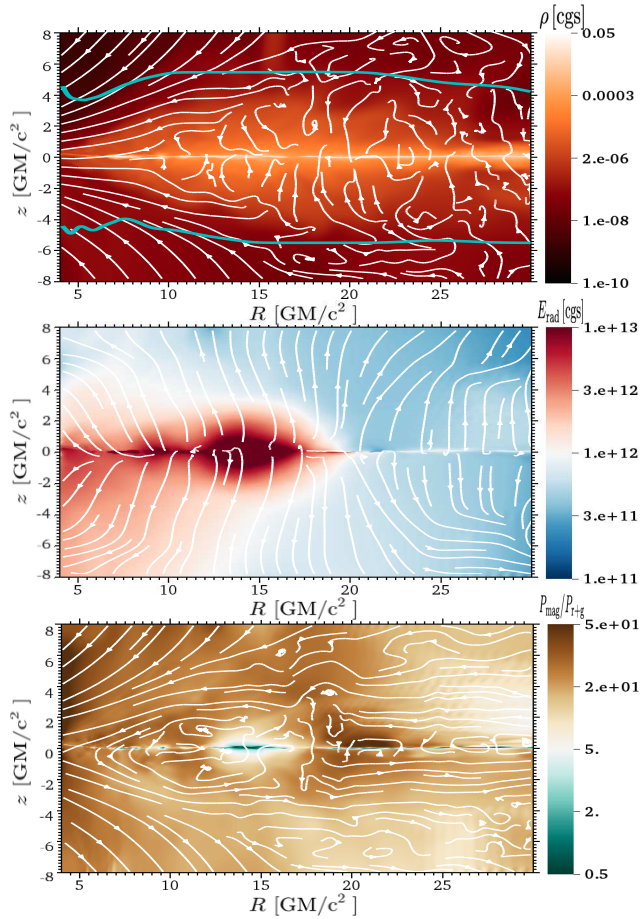


**Figure 2.** An  $R - z$  slice of the three-dimensional simulation, RADPHR. The panels show time averages over the last  $1000 \text{ GM}/c^3$  of the simulation. The top panel shows mass density with streamlines of azimuthally averaged fluid velocity. The photosphere is shown as a solid cyan curve. The middle panel shows the radiation energy, with streamlines of azimuthally averaged radiation velocity. The lower panel shows the ratio of magnetic pressure to the sum of radiation and gas pressures ( $P_{r+g}$ ), with streamlines of magnetic field.

$$t_{\text{cool}}(R) = \frac{\int \rho \epsilon dV}{Q^-} \quad (37)$$

where  $dV$  is the volume of a given radial shell *within the photosphere*. The numerator corresponds to the total thermal energy within this volume. The disc collapse negates the initial expansion such that the final height is at least a factor of five smaller than the initial one. We show a similar spacetime plot for the height of our low-resolution, RADPLR case in Fig. 4. Comparing Figs. 3 and 4, we see that it takes somewhat longer for the disc to collapse in our high-resolution simulation. It could be that at even higher resolution we might find that the disc will take even longer to collapse. This point will have to await future simulations.

The vertical collapse of the disc can also be seen in Fig. 5, which shows a spacetime plot of the radially and azimuthally averaged density as a function of height,  $z$ . The narrowing of the plot with time reflects the collapse of the disc. As the disc is collapsing, the photosphere (white curve) actually moves away from the mid-plane. This is because the opacity,  $\kappa\rho$ , goes roughly as  $\rho^2 T^{-7/2}$ . Thus, the rising density and falling temperature both drive the opacity of the gas up.

Another clue to the thermal state of the disc comes from look-

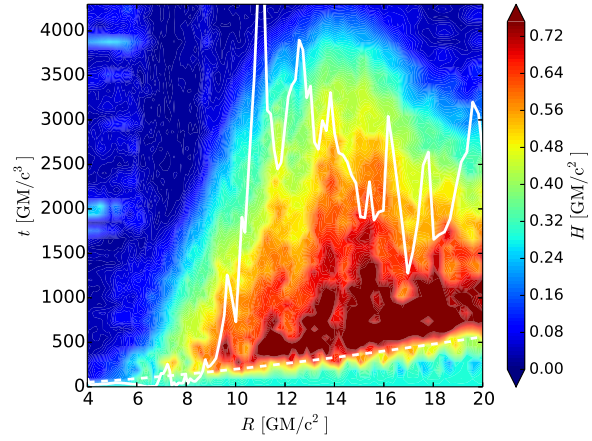


**Figure 3.** Spacetime plot for the azimuthally averaged, density-weighted height (31) of the disc in the high-resolution, RADPHR simulation. The dashed curve shows the local MRI growth time, while the solid curve shows a time average of the local cooling time (37).

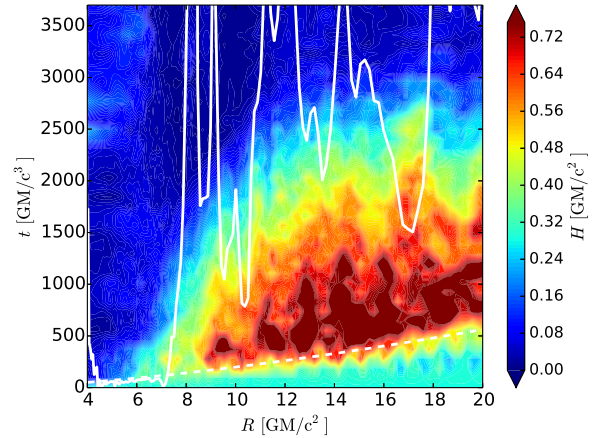


**Figure 4.** Same as Fig. 3, but for the low-resolution, RADPLR case.

ing at the time evolution of the local heating and cooling rates. In Fig. 6, we show a spacetime plot of the ratio of the heating rate to the cooling rate, computed using equations (33) and (34), respectively. The important takeaway is that cooling dominates over heating everywhere in the disc until after the disc has collapsed, when heating appears to dominate. Heating also dominates over cooling inside the ISCO, but this has little impact on our results.

The crucial question, though, is whether the disc collapses due to a true thermal instability. To assess this, we need to look at how the heating and cooling rates respond to changes in the total mid-plane pressure, which we do in Figs. 7 and 8. Fig. 7 seems to indicate that there is very little correlation between the bulk heating rate in the disc and the mid-plane pressure. Fig. 8, on the other hand, shows a strong, *positive* correlation between the cooling rate and the mid-plane pressure. So, while cooling has clearly dominated over heating during the evolution of model RADPHR (and RADPLR), this dominance weakens as the disc collapses. It appears that, at some point, heating will become more important than cooling. There are already some signs of this in Fig. 6 at late times.

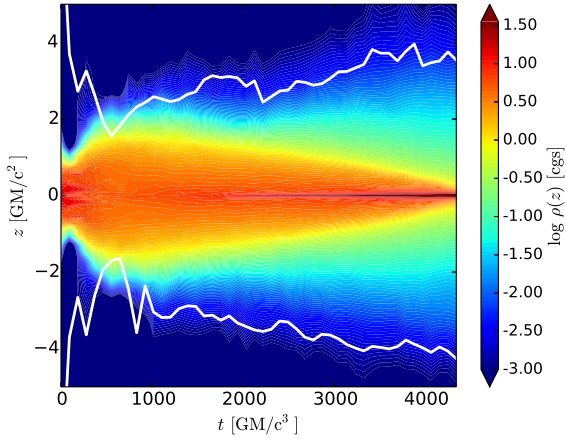


**Figure 5.** Spacetime plot of the vertical profile of the radially ( $R < 20$ ) and azimuthally averaged mass density for the collapsing disc in the RADPHR simulation. The white curves show the radially and azimuthally averaged photosphere height.

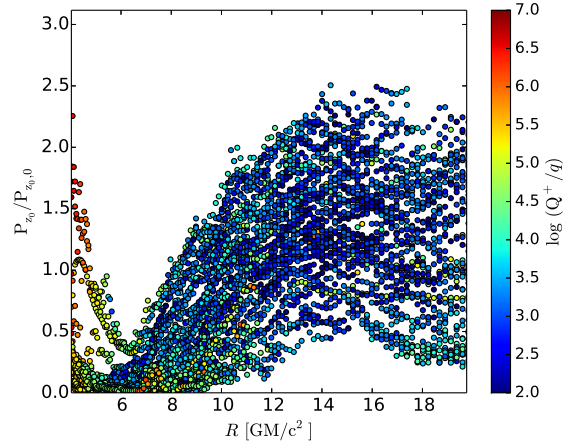


**Figure 7.** Scatter plot of the heating rate as a function of the azimuthally averaged, total, mid-plane pressure,  $P_{z0}$ , for the RADPHR simulation. The heating rate is normalized by  $q = 0.21H^3 P_{z0,0}\Omega$ , where  $H = 0.4r_g$ , while the mid-plane pressure is normalized by its initial value,  $P_{z0,0}$ .

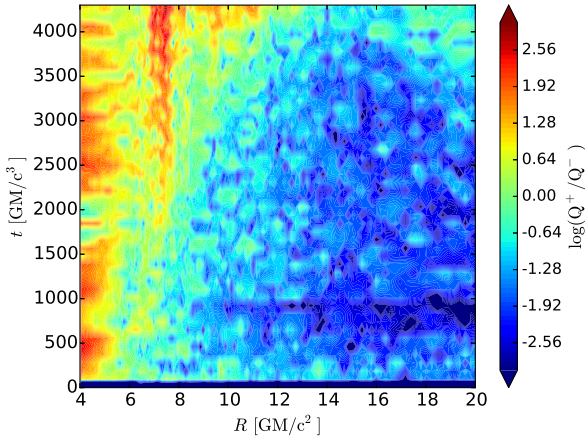


**Figure 6.** Spacetime plot for the ratio of the heating rate,  $Q^+$  (33), to the cooling rate,  $Q^-$  (34), for the RADPHR simulation.

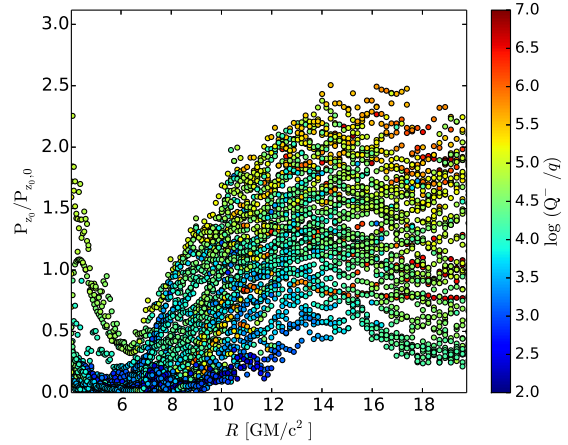


**Figure 8.** Scatter plot similar to Fig. 7, but for the cooling rate,  $Q^-$ .

This suggests that the disc is actually evolving toward a thermally *stable* solution.

In Fig. 9, we show the surface density,  $\Sigma$ , of the disc. This illustrates that  $\Sigma$  remains nearly constant throughout the simulation. This is important as it ensures that the disc collapse is not due to matter being drained into the black hole.

As mentioned at the beginning of this section, the RADPHR and RADLR simulations are initialized with the disc being radiation pressure dominated. In Fig. 10 we show that it remains so throughout the simulation. Obviously the region inside the ISCO is strongly radiation pressure dominated. This is not surprising as this region is largely devoid of gas, but filled with radiation (compare the top and middle panels of Fig. 2).

### 3.3 Gas-pressure-dominated disc

In the previous section we identified that our radiation-pressure-dominated thin disc is unstable to collapse. In this section, we contrast that result with a baseline, gas-pressure-dominated simulation.

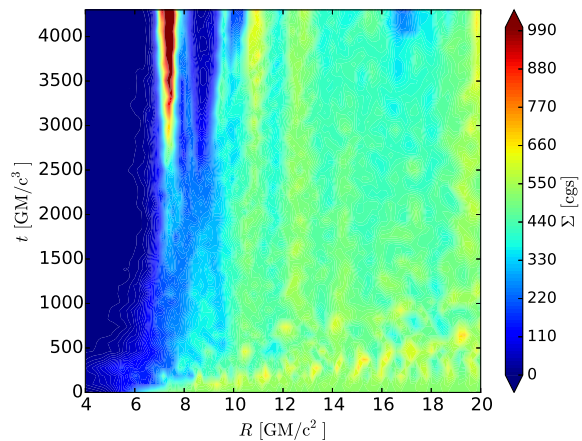


**Figure 9.** Spacetime plot for the surface density,  $\Sigma$ , of the disc in the RADPHR simulation.

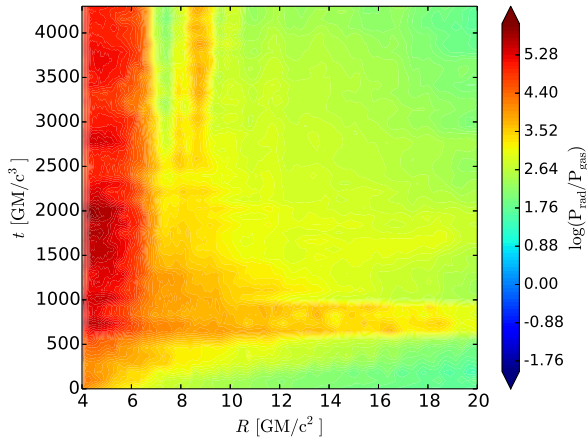


**Figure 10.** Spacetime plot of the ratio of the density-weighted, shell-averaged radiation pressure,  $P_{\text{rad}}$ , to gas pressure,  $P_{\text{gas}}$ , for the RADPHR simulation.

The primary goal in performing this simulation is to ensure that the result of the previous section is not a numerical artifact and that, indeed, our numerical setup is able to evolve stable thin disc configurations for sufficiently long duration. Here we focus on the low-resolution simulation, GASPLR, as it ran for significantly longer than its high-resolution counterpart. Even so, it did not run long enough to achieve inflow equilibrium through much of the radial domain. If the goal was really to understand the behavior of this disc, then this simulation should be run even longer. However, we were able to run it for many thermal times, long enough to provide a convincing counter-example to our collapsing disc.

We start with a spacetime plot of the disc height (Fig. 11), comparable to Figs. 3 and 4. In it we see that the region inside of  $\approx 16r_g$  maintains a nearly constant height following the onset of the MRI (dashed line). The local cooling time for this setup is of the order of  $0.01 GM/c^3$ , which is much shorter than in the radiation-pressure-dominated case. This is due to the fact that this setup has a mid-plane density three orders of magnitude lower than RADP. Also, the maximum mid-plane temperature for this setup is two orders of magnitude higher than RADP case. However, the GASPLR simulation does exhibit some thinning in its outer regions, an effect that was also seen in the radiation-pressure-dominated simulations. We suspect this is due to the fact that the MRI is not sufficiently well resolved in those regions (see Sec. 3.4), which allows cooling to dominate.

In Fig. 12 we show a space-time plot of the ratio of heating to cooling in the GASPLR case. We see that heating and cooling are nearly in balance over time over most of the disc. However, in the outer regions and at late times, there are parts of the disc where cooling dominates. As with the collapsing scale height in these regions, we attribute this behavior to the under resolved MRI.

In Fig. 13 we show the vertical profile of the radially and azimuthally averaged mass density for the GASPLR simulation. As with Fig. 11, we find that the gas-pressure-dominated disc maintains its height much better than the radiation-pressure-dominated one. The growth in the mid-plane density at late times is dominated by the thinning of the outer regions ( $R > 20$ ) of the disc (also seen in Fig. 11). The photosphere height (white curves) is also much more stable in this case.

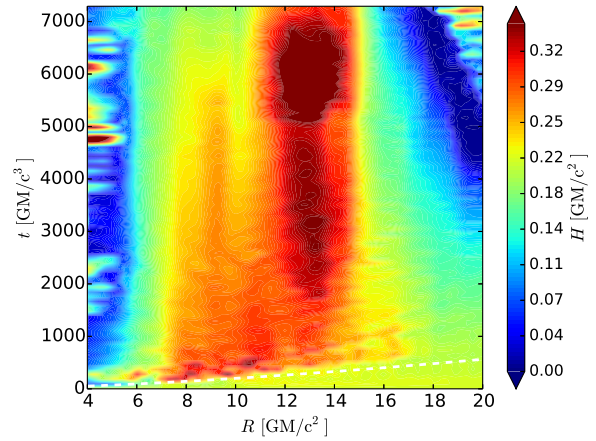


**Figure 11.** Same as Fig. 3, but for the GASPLR simulation. The local cooling time in this simulation is too short to be included in this plot.

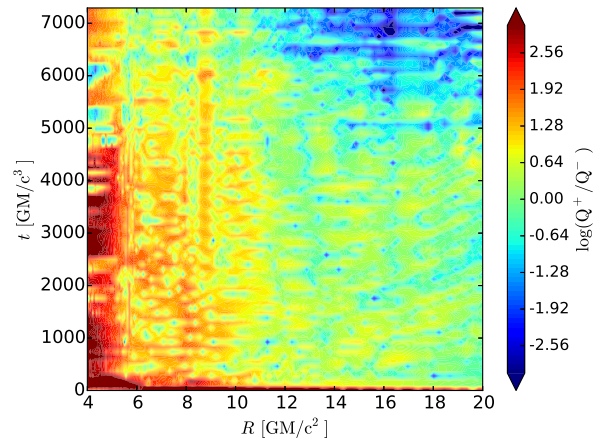


**Figure 12.** Same as Fig. 6, but for the GASPLR simulation.

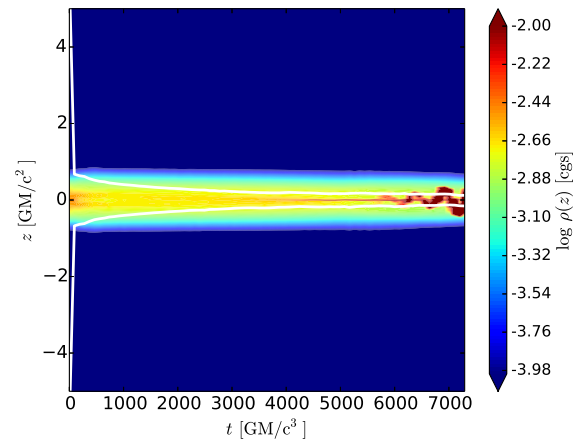


**Figure 13.** Same as Fig. 5, but for the GASPLR simulation.

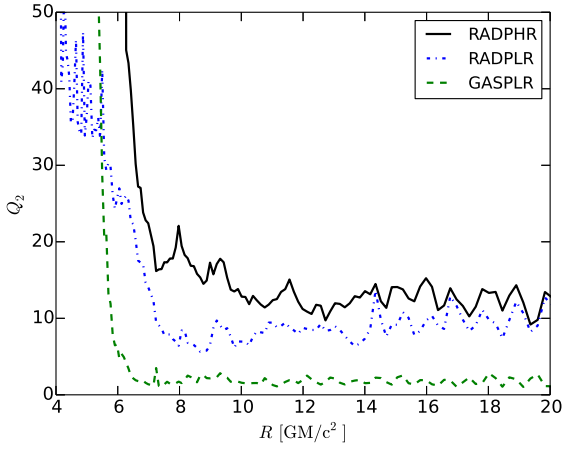


**Figure 14.** Time-averaged radial profile of the vertical MRI  $Q$  parameter,  $Q_2$ , for simulations RADPHR, RADPLR, and GASPLR.

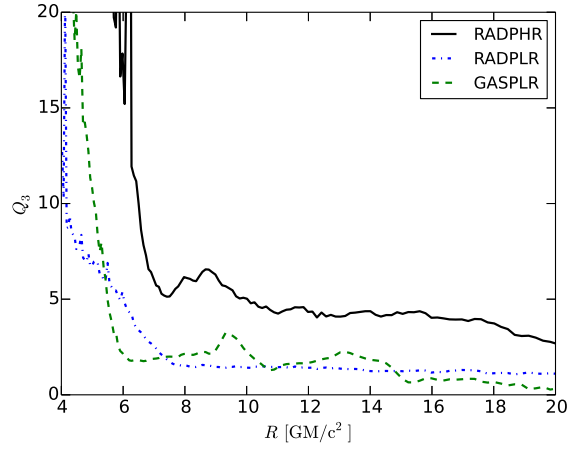


**Figure 15.** Time-averaged radial profile of the azimuthal MRI  $Q$  parameter,  $Q_3$ , for simulations RADPHR, RADPLR, and GASPLR.

### 3.4 Caveats

One major concern in performing numerical simulations of very thin accretion discs is resolving the MRI. Multiple resolution studies have shown that nearly all global simulations done to date have been under-resolved in this regard (e.g. Hawley, Guan & Krolik 2011; Hawley et al. 2013). A particular worry in our case is that under-resolving the MRI might cause the disc to collapse due to insufficient heating. Admittedly, as we show, some of our simulations fall below the ideal resolution. This is an unfortunate limitation of trying to perform global simulations, and doing so for thin discs only exacerbates the problem. However, an attempt to perform such thin disc simulation is necessary to make progress in understanding the physics of thin discs.

The standard measure of MRI resolution is the so-called  $Q$  parameter, defined as

$$Q_i = \frac{\lambda_{\text{MRI},i}}{\Delta x_i}, \quad (38)$$

where  $\lambda_{\text{MRI},i} = 2\pi v_{A,i}/|V^\phi|$  is the wavelength of fastest growing MRI mode,  $\Delta x_i$  is a typical zone length, and  $v_{A,i} = \sqrt{b_i b_i/\rho}$  is Alfvén speed, all in a given direction,  $i$ . We checked both the vertical (Fig. 14) and azimuthal (Fig. 15) MRI  $Q$  parameters for most of the models in Table. 1. For our radiation-pressure-dominated simulations, we actually capture the vertical MRI well, with  $Q_2 \gtrsim 10$  throughout most of the disc, especially in simulation RADPHR. The gas-pressure-dominated simulation is not nearly as well resolved, with  $Q_2 \lesssim 3$  at nearly all radii. The azimuthal direction is more problematic, with  $Q_3 \lesssim 5$ , even in the high-resolution RADPHR case. One way to possibly improve this in future simulations without requiring even more computational resources would be to reduce the azimuthal extent of the domain, while keeping the number of zones fixed. For now, we are left to point to the similarity of our results in both the low- and high-resolution simulations as evidence that the poor azimuthal MRI resolution does not negate our results of a thermal collapse in our radiation-pressure-dominated disc.

## 4 DISCUSSIONS AND CONCLUSIONS

These are among the first global simulations of geometrically very thin discs in general relativity to include radiation (see also Sądowski 2016). Our results are designed to be directly comparable to the shearing box simulations of Jiang, Stone & Davis (2013), thus extending their results to global simulations. The major conclusions of our paper are:

(i) As with previous shearing box (Jiang, Stone & Davis 2013) and global simulations with weak magnetic fields (Sądowski 2016), we find radiation-pressure-dominated thin discs to collapse. In our RADPHR simulation, cooling dominated over heating throughout the disc, at least until late times.

(ii) Our baseline gas-pressure-dominated simulation remained stable, with cooling and heating remaining roughly in balance throughout the disc. This confirms that our *Cosmos++* GRRMHD code is able to simulate stable, radiative, thin discs. It also supports the conclusion that the collapse we found in the radiation-pressure-dominated case is not a numerical artifact.

(iii) The fact that the radiation-pressure-dominated disc collapses on roughly the local cooling time also suggests that the collapse is not due to numerical effects, such as under-resolved MRI, though we readily admit that there is room for improvement in this area in our simulations, particularly in the azimuthal direction. However, a comparison of our low- and high-resolution simulations suggests that our main conclusions are robust.

It is not clear from our results, however, whether the collapse of our RADP simulations is due to a true thermal instability. Analysis of the dependence of our heating and cooling rates on the mid-plane pressure (Figs. 7 and 8) suggests it is not. Instead, the disc appears to be moving toward an even thinner, but possibly stable, final state. This highlights the importance of carefully analyzing the thermodynamics of radiation MHD simulations of thin discs.

As with any numerical study, there are caveats to our results. We have only studied the stability of two disc configurations for relatively short evolution times. A broader parameter study with longer simulations will be required to make our conclusions more robust. However, these simulations are very expensive computationally, so a broader study will have to wait.

## 5 ACKNOWLEDGMENTS

The research was supported by Polish NCN grants 2014/15/N/ST9/04633 and 2013/08/A/ST9/00795. This research was also supported by the National Science Foundation under grant NSF AST-1211230. Simulations were done using PROMETHEUS supercomputer in the PL-Grid infrastructure. B.M. is also thankful to the College of Charleston for hosting him during the initial stages of this project. B.M. and P.C.F. thank the International Space Science Institute, where part of this work was carried out, for their hospitality.

## REFERENCES

- Anninos P., Fragile P. C., Salmonson J. D., 2005, *ApJ*, 635, 723  
Balbus S. A., Hawley J. F., 1991, *ApJ*, 376, 214  
Begelman M. C., Pringle J. E., 2007, *MNRAS*, 375, 1070  
Brandenburg A., Nordlund A., Stein R. F., Torkelsson U., 1995, *ApJ*, 446, 741  
Fragile P. C., Gillespie A., Monahan T., Rodriguez M., Anninos P., 2012, *The ApJS*, 201, 9  
Fragile P. C., Olejar A., Anninos P., 2014, *ApJ*, 796, 22  
Hawley J. F., Guan X., Krolik J. H., 2011, *ApJ*, 738, 84  
Hawley J. F., Richers S. A., Guan X., Krolik J. H., 2013, *ApJ*, 772, 102  
Hirose S., Krolik J. H., Blaes O., 2009, *ApJ*, 691, 16  
Jiang Y.-F., Stone J. M., Davis S. W., 2013, *ApJ*, 778, 65  
Lightman A. P., Eardley D. M., 1974, *ApJL*, 187, L1  
Oda H., Machida M., Nakamura K. E., Matsumoto R., 2009, *ApJ*, 697, 16  
Piran T., 1978, *ApJ*, 221, 652  
Ressler S. M., Tchekhovskoy A., Quataert E., Chandra M., Gammie C. F., 2015, *MNRAS*, 454, 1848  
Reynolds C. S., Miller M. C., 2009, *ApJ*, 692, 869  
Sądowski A., 2016, *ArXiv e-prints*  
Sądowski A., Narayan R., Tchekhovskoy A., Zhu Y., 2013, *MNRAS*, 429, 3533  
Shakura N. I., Sunyaev R. A., 1973, *A&A*, 24, 337  
Shakura N. I., Sunyaev R. A., 1976, *MNRAS*, 175, 613  
Stone J. M., Hawley J. F., Gammie C. F., Balbus S. A., 1996, *ApJ*, 463, 656  
Turner N. J., 2004, *ApJL*, 605, L45